Northumbria Research Link

A New Cooling Rate Dependent Machine Learning Feature for the Design of Thermally Sprayed High Entropy Alloys

SCHOLARONE™
Manuscripts

1
2
3
4
5
6
7
8
9
10
11
12
13
14
15
16
17
18
19
20
21
22
23
24
25
26
27
28
29
30
31
32
33
34
35
36
37
38
39
40
41
42
43
44
45
46
47
48
49
50
51
52
53
54
55
56
57
58
59
60

A New Cooling Rate Dependent Machine Learning Feature for the Design of Thermally Sprayed High Entropy Alloys

S. Kamnis[1*], A.K. Sfikas[2], S. Gonzalez[2] A.E. Karantzalis[3], E. Georgatis[3]

Contact Email: spyros.kamnis@castolin.com

[1] Castolin Eutectic-Monitor Coatings, Newcastle, United Kingdom

[2] Faculty of Engineering and Environment, Northumbria University, Newcastle, United Kingdom

[3] Department Materials Science and Engineering, University of Ioannina, Ioannina, Greece

*Corresponding Author

Abstract

Highly accurate machine learning (ML) approaches rely heavily on the quality of data and the design features that are used as inputs to the model. The applicability of these methods for phase formation predictions is questionable when it comes to the design of thermally sprayed high entropy alloy (HEA) coatings using gas or water atomized powders as feedstock material. Phase formation from liquid state depends on the cooling rate during atomization which is several orders of magnitude higher when compared to arc melted as-cast HEAs. In addition, during plasma spray the powder melts in the flame and re-solidifies under different cooling rates during deposition. To our knowledge, almost all ML algorithms are based on available datasets constructed from relatively low cooling rate processes such as arc melting and suction casting. A new approach is needed to broaden the applicability of ML algorithms to rapid solidification manufacturing processes similar to gas and water atomization by making use of existing data and theoretical models. In this study the authors introduce a cooling rate dependent design feature that can lead to accurate predictions of the HEA powder phase formation and the subsequent phases found in the spray coated materials. The model is validated experimentally and also by comparing the predictions with existing coating related data in the literature.

Keywords: High Entropy Alloys, Machine Learning, Cooling Rate, Thermal Spray

1
2
3
4
5
6
7
8
9
10
11
12
13
14
15
16
17
18
19
20
21
22
23
24
25
26
27
28
29
30
31
32
33
34
35
36
37
38
39
40
41
42
43
44
45
46
47
48
49
50
51
52
53
54
55
56
57
58
59
60

1. Introduction

Traditional alloying strategies are based on the use of a principal element to satisfy the need for primary properties and the inclusion of secondary elements in small amounts to enhance other properties. However, back in 2004, two different groups working in parallel published works on the development of a different approach creating single phase materials by using multiple different elements leading to the creation of high-entropy alloys (HEAs) (Ref 1,2) and multicomponent alloys (Ref 3) . HEAs are defined as systems composed of 5 or more elements with concentrations for each element between 5-35 at.% and exhibit four core effects: high entropy, lattice distortion, sluggish diffusion and the cocktail effects (Ref 4,5).

HEAs have received significant attention for their superior mechanical properties such as hardness, ductility, and corrosion resistance over those of conventional alloys (Ref 6-11) and recently, the concept of HEAs has extended into functional materials, such as catalytic materials for hydrogen production, thermoelectric materials, and coating materials (Ref 12-24). In the field of surface engineering and advanced coatings, HEAs provide a transformative opportunity to design surfaces that are custom tailored to the distinct needs of a given application. HEAs deliver new options to manufacturers to produce alternatives to materials that are rare, hazardous, expensive, subject to international restrictions and are designed around the limitations of current materials that form part of a 30-year-old legacy.

Multicomponent and HEA materials offer a pluralism in terms of physical, chemical, and mechanical properties, making them promising for a variety of applications. However, the large composition space introduces new challenges for designing novel HEAs with tailored properties or functionalities. The typical trial-and-error approach cannot be applied due to the considerable time and cost for the investigation of the vast amount of possible compositions.

Throughout the years, parametric and computational approaches have been used extensively for the design of HEAs. The parametric approach is based on empirical rules established from the analysis of theoretical models and design parameters known so far, e.g., atomic size difference δ, mixing entropy ΔSmix, mixing enthalpy ΔHmix, valence electron concentration (VEC), electronegativity difference Δχ and itinerant electron concentration (e/a) (Ref 25-30). Maps based on these parameters were built to single out regions in the parameter space corresponding to alloys which were known experimentally to be single phased. The maps proved useful in rationalizing the findings on HEA systems known at the time and have become a tool for predicting the phases occurring in new systems. There are obvious exceptions in the maps, as shown in the next section, which suggests further analyses and research that could potentially lead to better predictive models, especially when powder atomisation is used implying rather fast solidification which may lead to non-equilibrium microstructural outcomes.

In this direction, computational approaches, e.g., Calculation of Phase Diagrams (CALPHAD), molecular dynamics simulation, and first-principles density functional theory calculations, have been utilized to estimate under what conditions a specific phase is formed and to predict structural and electronic properties of HEAs based on previous experimental data (Ref 31). Those conventional approaches, however, have limitations due to excessive computational costs and high uncertainties (Ref 32). In the CALPHAD technique for example, Gibbs energy models with parameters describing each phase in a multicomponent system are obtained based on experimental and first principles information. On the contrary, HEAs are positioned in the central regions of multidimensional phase diagrams, well outside the limits usually used to construct energy model parameters through databases. As a result, calculations in large composition spaces require large extrapolations from the classical thermodynamic models which may lead to inaccurate evaluations of the Gibbs energies and phase equilibria.

Reliability and accuracy of the predictions can thus become questionable when obtained from incomplete thermodynamic descriptions(Ref 33).

To address the aforementioned limitations, over the recent years, machine learning (ML) has been applied in the field of HEAs as a data-driven approach. Machine learning methods are known for their feature learning ability from data representation using complex neural network architectures towards a global approximation of nonlinearity. With the recent HEA data accumulation, several works have shown promising results for estimating phases and mechanical properties of such complex systems (Ref 34-38). Current limitations of ML methods include pure regularisation and overfitting, the generalisation ability of most models is questionable due to the lack of powerful feature descriptors (i.e., meaningful thermodynamic inputs), and the poor interpretation of neural network target outcomes. Another critical limitation that renders ML approaches less effective for thermal spray feedstock HEA material design is the lack of information in most datasets regarding the manufacturing process and the critical cooling rates. It is also important to note that phase formation from liquid state depends on the cooling rate during solidification and approaches involving phase transformation of alloys that depend on the cooling rate are rare in the literature (Ref 39). In the field of thermal spray, it is important to develop a model which can predict whether a given elemental combination in equiatomic or near equiatomic proportion will form a particular solid solution (SS) phase depending on the cooling rate during solidification of liquid in gas or water atomisers and the subsequent re-melting and solidification during the spray coating deposition.

In this work the authors present a Random forest ML approach (Ref 40). Random forests are composed of an ensemble of decision trees. Decision trees are simple models that recursively partition the input space and define a piece-wise function, typically constant, on the partitions. Single decision trees often have poor predictive power for non-linear relations or noisy data sets. In random forests, these weaknesses are overcome by using an ensemble of

decision trees, each one fit to a different random draw, with replacement, of the training data set. For a given test point, the predictions of all the trees in the forest are aggregated, usually by taking the mean. The Random Forest model has been selected because of its robustness when dealing with high dimensional data and its ability to handle effectively unbalanced data. Random forest tries to minimize the overall error rate, so in the presence of an unbalance data set, the larger class will get a low error rate while the smaller class will have a larger error rate. Finally, each decision tree has a high variance, but low bias. The random forest classifier was implemented with Scikit-learn (Ref 41). Its superior performance in other materials science studies, where data is often limited, has been demonstrated in previous studies (Ref 42,43). This work builds on previous ML approaches while introducing a critical new feature descriptor that enables the prediction of phase formation in atomised powder feedstock materials and coatings. The cooling rates during powder manufacturing can be as high as 10^{10} K/s (Ref 44) and the rapid particle re-solidification upon impact on the substrate during spray can reach cooling rates up to 10^8 K/s (Ref 45).

2. Dataset, Features and Model Description

2.1 Dataset Analysis

The datasets were constructed from several previous works (Ref 5,35,43) and used to develop the present Random Forest based phase prediction model. After minor data cleaning for the elimination of redundant samples, the dataset was finalised with a total of 133 samples classified into phases including FCC, BCC and HCP as found in the dataset that was constructed from the information provided in (Ref 39). The total number of equiatomic compositions is 45 with each one associated to experimentally observed phase formation under three different cooling rates.

Besides the design parameters based on empirical rules, i.e., δ, ΔSmix, ΔHmix, VEC, and Δχ (Ref 25,36,39), the authors capitalize on the work by Chattopadhyay et.al. (Ref 39), where phase formation predictions are obtained from temperature-time-transformation (TTT) diagrams for different alloy cooling rates.

To explore and assess the feature distribution of the dataset, visualization of the feature representation of all samples in two dimensions is achieved using the t-stochastic neighbour embedding (t-SNE) method (Ref 46). A total of 13 design parameters indicate 13 dimensions of the feature space that are fed into the model. In Figure 1, the high-dimensional data are embedded into the low-dimensional space. The data maintain their original characteristics of distance similarities among data points with the two-axis having no physical meaning. The embedded distributions of a multiphase system, FCC+BCC for example, appears to be significantly entangled, as shown in Figure 1a, when the cooling rate information are incorporated without further feature engineering. This implies that similar feature representations co-exist in the original feature space making it difficult to distinguish between them for the cooling rate dependent phase predictions as opposed to datasets constructed without significant cooling rate variations (Figure 1b).

As it is further demonstrated in Figure 2, there are samples in the dataset that share very similar individual or combinatorial principles that stem from thermodynamic empirical rules but exhibit different phase formations. This is an expected behaviour since the empirical rule descriptors are de-coupled from the solidification mechanisms and their effect on phase formation. Figure 2, shows a scatter plot between the mixing-rule calculated Ionisation Energy and the mixing-rule calculated Latent Heat for the alloys in the dataset for the existing FCC+BCC and Other cases. The pair-plot visualisation of all features against all samples suggest that the feature representation is ambiguous when cooling rates are employed leading to significant number of misclassification cases particularly in multi-phase systems.

Accordingly, our goal is to succeed in nonlinear mapping that differentiates those feature distributions of all phases via a new cooling rate related design feature.

2.2 Feature Construction

It has been demonstrated by several works (Ref 47-50) that the phases formed in HEAs are in several cases the outcome of phase separation, leading to an inherited from lower order alloy phase formation. It is also important to note that phase formation from liquid state depends on the cooling rate during solidification. Therefore, it is of immense importance to develop a new design feature that would be fed into Neural Networks, Decision Trees and Random Forest models. The new design feature should consider thermodynamic and crystal structure information coupled with solidification kinetics of a given composition.

The temperature dependence of the viscosity n of the HEA melt ZrTiCuNiBe has been provided in (Ref 39) and fits the experimental $\ln n \sim \frac{1}{T}$ relationship in the form:

$$\ln n = A + B\left(\frac{Tm}{T}\right)^a \tag{1}$$

where A, B and a are constants, with a being a material composition dependent parameter and Tm the alloy melting point. It has been obtained experimentally by (Ref 51) that the cooling rate (q_c) relationship $\frac{1}{q_c} \sim \frac{Tm}{T}$, in a wide range of cooling rates (K/s), is fitted by the equation:

$$\ln \left(\frac{1}{q_c}\right) = A' + B\left(\frac{Tm}{T}\right)^a \tag{2}$$

where B and a are also shown in Eq. 1 and A' is a fitting adjusting parameter. Subtracting Eq. 1 from Eq. 2 we get:

$$\ln q_c = \ln S_k - \ln n \tag{3}$$

$$q_c = \frac{S_k}{n} \tag{4}$$

The S_k (MPa K) is the new design feature introduced in this study which is a shift factor making the equivalent Eq.1 and Eq.2 to overlap. It is expected all phases to have different temperature dependent viscosity behaviour due to their different packing fractions. Feeding the S_k values into the ML algorithm, new similarity pattern exploration is possible by creating dissimilar feature representations for phase formation under different solidification rates.

The viscosity of an alloy can be estimated using classic Grunberg-Nissan (Ref 52) mixing rule for liquid mixture (Eq. 5):

$$\ln n = \sum_{i=1}^{N} x_i \ln n_i \tag{5}$$

or more complex expressions (Eq. 6) such as the Budai et al. (Ref 53)

$$n = \frac{h \cdot N_A}{\sum x_i \cdot V_m^i + \Delta V_m^E} \cdot exp\left[\frac{(\sum x_i \cdot \Delta G_i^*) - 0.155 \cdot \Delta H}{R \cdot T}\right] \tag{6}$$

where h is the Planck constant, N_A is the Avogadro number, V_m the molar volume of the element i, ΔV_m^E is the excess molar volume upon alloy formation and is set to zero in the absence of data, ΔH is the mixing enthalpy calculated by using Miedema's model (Ref 54) and ΔG_i^* is the Gibbs energy of activation of the viscous flow in pure component i and can be expressed as:

$$\Delta G_i^* = R \cdot T \cdot ln\left(\frac{n_i \cdot M_i}{h \cdot N_A \cdot \rho_i}\right) \tag{7}$$

where, ρ_i is the density of the element i, M_i is the atomic weight of the element i and n_i is the individual element viscosity. Substituting Eq.7 into Eq.6 we get the final viscosity expression that contains crystal structure information in the density term that theoretically is expressed as:

$\rho = \frac{N_C M}{V_c N_A}$, where N_C and V_c are the effective number of atoms per unit cell and volume of unit cell of the material. The elemental viscosities can be calculated from (Ref 55-57).

The new feature finally takes the following form using Eq. 4:

$$S_k = q_c \frac{h N_A}{V_{alloy}} exp\left[\frac{\Delta G_{alloy} - 0.155 \cdot \Delta H_{mix}}{R T_m}\right] \qquad (8)$$

The model is based on the assumption that similar temperature dependent viscosity and cooling rate behaviours govern the majority of equiatomic HEA systems, regardless of their composition and number of individual elements.

3. New Feature Evaluation

For the random forest classifier implemented with Scikit-learn, model hyper-parameters are selected via an exhaustive 3-fold cross-validated grid search using the following parameters: number of tree predictors in range 11 to 111 in steps of 10, the number of features considered at each split, and scoring based on gini (a measure of impurity) as model performance criterion. To avoid the effects of collinearity (highly correlated features) and dimensionality, 3-fold cross validated recursive feature elimination (RFECV) is performed before the grid search through the hyperparameters. The best performing hyper parameters were selected to fit a model using the entire training set, with bootstrap aggregation applying each decision tree a random subset containing approximately 2/3 of the data, to maximize the amount of information available for making future predictions.

The feature importance (Table 1) was extracted for the model using the Citrination platform (available at http://www.citrination.com last access: 07 March 2022). The feature

importance was ranked by observing the effect on model accuracy by randomly permuting the values of each feature. This is done to measure the impact of swapping the value of a selected feature from one composition with the value from a different composition. It is evidently shown that the newly constructed S_k feature (Eq.8) is ranked first among several standard ML HEA predictors found in the literature.

The model accuracy presented in Table 2 is estimated by tallying and reporting the percentage of predictor trees that "vote" for each of the output phases (none/neither, face-centered cubic, or body-centered cubic) for each input composition. The model achieves an accuracy of 81%. The same accuracy is observed from the Receiver Operator Characteristic (ROC) curve in Figure 3. The ROC curve is a graphical plot used to show the diagnostic ability of binary classifiers. It shows the trade-off between sensitivity (or TPR) and specificity (1 − FPR). Classifiers that give curves closer to the top-left corner indicate a better performance. As a baseline, a random classifier is expected to give points lying along the diagonal (FPR = TPR). The closer the curve comes to the 45-degree diagonal of the ROC space, the less accurate the test.

Figure 4 graphically defines the input space (VEC and S_k), decision regions (1 = FCC, 0 = BCC), and decision boundaries for a two-dimensional binary classification problem. Interpreting the decision map, one can conclude that FCC phase formation is expected for S_k values between 0 and 1 and for VEC values larger than 7. Increased probability of a BCC phase formation for $S_k > 1$ in the $8 > VEC > 7$ range is observed while for $VEC > 8$ the FCC phase suppression due to rapid solidification is less likely to occur.

The new feature from this work was implemented alongside 13 thermodynamic parameters as model inputs in a larger dataset including 511 compositions where the cooling rates were approximated based on the production method. The model achieves the same accuracy of 81%

and the confusion matrix (Figure 5) shows very good diagonal distribution of correctly classified phases. The confusion or error matrix is a specific table layout that allows visualization of the performance of an algorithm. Each row of the matrix represents the instances in an actual class while each column represents the instances in a predicted class. In Table 3, the model predictions are compared to as-cast materials, atomized powders and the resulting coatings. The final phase formation depends on several other parameters and the new S_k feature should be used alongside other empirical rules as listed in Table 1. This is because the final phase formation predictions depend on the trained model input weights.

4. Experimental Validation & Discussions

This work suggests that kinetics is an important consideration that may affect the microstructure and the properties of HEAs in line with previous observations in the literature. Lobel et al. (Ref 58) reported that AlCoCrFeNiTi0.5 fabricated by gas atomisation consisted of two BCC phases. The fast-cooling rate suppressed the segregation of the melt and led to the suppression of the FCC phase. Subsequent Spark plasma sintering of the gas atomised powder led to the formation of additional phases, sigma and FCC. Chen et al. (Ref 59) studied the effect of the cooling rate on the microstructure and mechanical properties of a vacuum arc melted CrFeCoNiAl0.6 that was subsequently remelted in copper molds of various diameters. According to the results, the cooling rate can control the fraction of BCC phase and the refinement of FCC allowing to tune the mechanical properties. He et al. (Ref 60) investigated the kinetic effect on the phase transformation and selection of a CoCrFeNiTi0.4 HEA. Under low cooling rate the microstructure consists of FCC, sigma, R and γ´. However, extremely rapid solidification led to the suppression of the formation of sigma, R and γ´. It was deducted that solidification rate and solid-state transformation kinetics could be used to control the phase selection of HEAs for improved performance.

Taking into account the S_k and VEC pair rules shown in Fig. 4 the modified CoCrFeMnNi$_{0.8}$V Cantor alloy (CantorV) with VEC = 7.4 was selected for validation purposes and compared alongside the original Cantor CoCrFeMnNi system (VEC=8). Both the Cantor and CantorV bulk samples were fabricated with the use of pieces of elements of high purity (99.9 wt.%) with the employment of an Edmund Buhler MAM-1 compact arc-melter. Proper quantities of the raw materials were measured with the use of a Fisherbrand analytical balance and then ultrasonically cleaned. Afterwards, they were inserted in the chamber and melted under Ar to acquire the master alloy. The master alloy was suction casted into a water-cooled Cu mold with diameter of 8 mm and length of 30 mm. The cylindrical samples were cut in smaller pieces and were subject to standard metallographic procedures in order to study the microstructure. The mixing rule viscosities for the two alloys were calculated using Eq.5. The equivalent S_k values for the bulk arc-melted alloys based on Eq. 4 are S_k = 0.000045 for the CantorV and S_k = 0.000047 for the original Cantor alloy for a cooling rate equal to 1000K/s.

To test the response of the two alloys under very rapid solidification atomized powders were produced and analyzed. The calculated S_k value is 1.13 for the CantorV alloy (atomization cooling rate ≈ 2.5 x 10^8) and S_k = 0.93x108 for the original Cantor alloy (atomization cooling rate ≈ 2 x 10^8). The cooling rates were estimated based on the atomization process parameters and established break-up and solidification models (Ref 39,61,62). Based on the VEC and S_k values, this study suggests and confirms that the CantorV alloy will not retain the FCC structure during atomization since the S_k value is higher than 1 and the material VEC is below 8. On the contrary, the original Cantor alloy is expected to sustain the FCC structure (S_k < 1, VEC=8)) after atomization.

The produced powders were then used as feedstock material for typical atmospheric plasma spray (APS) and High Velocity Oxy-Fuel (HVOF) thermal spray. The HVOF spray system is designed by Castolin Eutectic-Monitor Coatings Ltd. (North Shields, UK), utilizing

both air and oxygen alongside the fuel for combustion. The plasma coatings were applied using the 3MB torch by Oerlikon Metco in a dedicated NADCAP certified aerospace booth at Monitor Coatings Ltd in the UK. The torch delivers up to 50KW of power and plasma temperatures up to 16,000 ºC, gas velocities up to 3,000m/s and particle acceleration up to 600m/s. The torch was mounted on a robotic arm and the samples were sprayed using a raster scan program.

The coatings were deposited on S275 steel plates (nominal composition: C< 0.25 wt.%, Mn< 1.6 wt.%, S< 0.05 wt. %, P< 0.04 wt.%, Si< 0.05 wt.%) of 50x50 mm and 6 mm thickness traversing the gun linearly (raster scan pattern) using a robotic arm. The spray angle was fixed at 90 degrees and the gas flow rates were controlled using a digital console. The suction casted samples, the gas atomized powder and the coatings were studied with the employment of a Rigaku Smartlab SE X-ray diffractometer (CuKa radiation, standard split) and a Tescan Mira 3 scanning electron microscope equipped with an Oxford Instruments EDS analyser. X-ray diffractograms were acquired with a step size of 0.01 □/s.

Figure 6 presents the X-ray diffractograms of the suction cast bulk CoCrFeMnNi and CoCrFeMnNi$_{0.8}$V and corresponding elemental maps. According to the results, the CoCrFeMnNi$_{0.8}$V fabricated by suction casting consists of two phases as opposed to the CoCrFeMnNi that shows a single FCC structure (Fig.6a). The sigma phase (Light grey phase) and an FCC solid solution (Dark grey phase) are shown in Figure 6b. Sigma is enriched in Cr, V and depleted in Mn, Ni. On the other hand, the FCC solid solution is enriched in Mn, Ni and depleted from Cr, V. The chemical composition and phase formation of the bulk as-cast, powder and coating materials are summarized in Table 4.

The gas atomized CoCrFeMnNi$_{0.8}$V particles consist of a single BCC solid solution (Fig. 7a), as opposed to the as-cast FCC + sigma phases, with an average size of 20-50 μm

while the CoCrFeMnNi particles retain the FCC structure as observed in the as-cast material (Fig. 6a). The particles have a spherical and dense structured with no porosity or other defects such as satellite droplets, agglomeration and hollow structures (Fig.7b). The chemical composition of the powders is close to the nominal composition (Table 4) of the as-cast systems. The powder exhibits good distribution of the elements as shown in Fig.7c.

The CoCrFeMnNi and CoCrFeMnNi0.8V coatings were sprayed using the produced HEA powders on carbon steel substrates with the employment of two different techniques. During HVOF application the temperature for the 45μm average particle is approximately 1127 C and 1429 C respectively (Ref 12), lower than the melting point of the material (1584 C). On the other hand, the temperature for the average particle during atmospheric plasma spraying is well above the melting point of the material resulting in fully molten particle impingement and re-solidification as demonstrated in Figure 8a,b. The HVOF sprayed original Cantor alloy exhibits the same crystal structure in all production stages from bulk as-cast to powder and coating formation in line with the model predictions. The inconsistency of the microstructure between the bulk CoCrFeMnNi$_{0.8}$V, the gas atomized equivalent and the resulting Plasma coating as predicted by the model can be explained by analyzing the solidification and cooling rate sequences in conjunction with the S_k values and the VEC number of the alloy.

During atomization the S_k value is higher than 1 at VEC=7.4 and suppression of the FCC and sigma phases is expected. The BCC CantorV powder when sprayed under HVOF process temperatures does not undergo significant in-flight melting and thus no significant deviations from the feedstock composition is expected (Figure 9 a, b and Figures 6, 7). On the contrary, during plasma spray, the particles impact on the substrate at fully molten state and solidify rapidly to form the lamella structure shown in Figure 8 a,b. The re-solidification occurs at different speeds depending on the particle size. For this reason, several particles solidify faster than others resulting in different S_k values ranging from 0.1 to 1.2 MPa K. According to

this study and as shown in Figure 8a both FCC and BCC phases are predicted and experimentally verified in the coating. Larger particles are cooled down at lower rate delivering the same crystal structure as the feedstock material. The original Cantor alloy with a higher VEC number appears to be less prone to metastable phase formation and thus the FCC is retained regardless of the S_k value as suggested by the decision plot in Figure 4 and shown in Figure 8b.

5. Conclusions

In the field of thermal spray, it is important to develop a model which can predict whether a given multicomponent elemental combination will form a particular solid solution phase depending on the cooling rate during solidification of liquid metal in gas or water atomisers and the subsequent re-melting and solidification of the powder during the spray coating deposition. For this purpose, in this study a new design feature has been constructed and used as input to a random forest ML model to predict the phase formation of High Entropy Alloys under rapid solidification conditions. This approach is based on the viscosity of alloys as a function of temperature, utilising the viscosities of its constituting elements, and suitably incorporating the cooling rate information. The most important part of the present work is that it offers an additional design tool for thermal spray processes and the route that should be used to form an intended phase in a particular alloy via the critical S_k value. The phase formation in most of the coated alloys and their atomised feedstock material has been predicted correctly by the model. Higher cooling rates as denoted by $S_k > 1$ values in the composition range of $8 > VEC > 7$ may lead to the suppression of the FCC phase and the formation of a more open space BCC structure instead. Similarly, as shown in Table 3 and validated in Section 4 secondary phases are supressed when specific VEC and S_k conditions are satisfied after gas atomisation leading to the formation of single-phase powders as opposed to multi-phase as-cast materials.

References

1. B. Cantor, Multicomponent High-Entropy Cantor Alloys, *Prog. Mater. Sci.*, 2021, **120**(1), p 100754.

2. J.W. Yeh, S.K. Chen, S.J. Lin, J.Y. Gan, T.S. Chin, T.T. Shun, C.H. Tsau, and S.Y. Chang, Nanostructured High-Entropy Alloys with Multiple Principal Elements: Novel Alloy Design Concepts and Outcomes, *Adv. Eng. Mater.*, 2004, **6**(5), p 299–303.

3. B. Cantor, I.T.H. Chang, P. Knight, and A.J.B. Vincent, Microstructural Development in Equiatomic Multicomponent Alloys, *Mater. Sci. Eng. A*, 2004, **375**, p 213–218.

4. J.W. Yeh, Recent Progress in High-Entropy Alloys, *Ann. Chim. Sci. des Mater.*, 2006, **31**(6), p 633–648.

5. D.B. Miracle and O.N. Senkov, A Critical Review of High Entropy Alloys and Related Concepts, *Acta Mater.*, 2017, **122**, p 448–511.

6. C. Li, J.C. Li, M. Zhao, and Q. Jiang, Effect of Alloying Elements on Microstructure and Properties of Multiprincipal Elements High-Entropy Alloys, *J. Alloys Compd.*, 2009, **475**(1–2), p 752–757.

7. A. Poulia, E. Georgatis, A. Lekatou, and A.E. Karantzalis, Microstructure and Wear Behavior of a Refractory High Entropy Alloy, *Int. J. Refract. Met. Hard Mater.*, 2016, **57**, p 50–63.

8. C. Mathiou, A. Poulia, E. Georgatis, and A.E. Karantzalis, Microstructural Features and Dry - Sliding Wear Response of MoTaNbZrTi High Entropy Alloy, *Mater. Chem. Phys.*, 2018, **210**, p 126–135.

9. K. Lentzaris, A. Poulia, E. Georgatis, A.G. Lekatou, and A.E. Karantzalis, Analysis of Microstructure and Sliding Wear Behavior of Co1.5CrFeNi1.5Ti0.5 High-Entropy Alloy, *J. Mater. Eng. Perform.*, 2018, **27**(10), p 5177–5186.

10. M.H. Chuang, M.H. Tsai, W.R. Wang, S.J. Lin, and J.W. Yeh, Microstructure and Wear Behavior of AlxCo 1.5CrFeNi1.5Tiy High-Entropy Alloys, *Acta Mater.*, 2011, **59**(16), p 6308–6317.

11. A. Parakh, M. Vaidya, N. Kumar, R. Chetty, and B.S. Murty, Effect of Crystal Structure and Grain Size on Corrosion Properties of AlCoCrFeNi High Entropy Alloy, *J. Alloys Compd.*, 2021, **863**, p 158056.

12. S. Kamnis, A.K. Sfikas, B. Allcock, and S. Gonzalez, HVOF Processed CoCrFeMnNi High-Entropy Alloy Coatings: A Combined Computational and Experimental Validation Approach, *J. Therm. Spray Technol.*, 2021, **31**(4), p 1000–1010.

13. J.K. Xiao, H. Tan, Y.Q. Wu, J. Chen, and C. Zhang, Microstructure and Wear Behavior of FeCoNiCrMn High Entropy Alloy Coating Deposited by Plasma Spraying, *Surf. Coatings Technol.*, 2020, **385**, p 125430.

14. K.C. Cheng, J.H. Chen, S. Stadler, and S.H. Chen, Properties of Atomized AlCoCrFeNi High-Entropy Alloy Powders and Their Phase-Adjustable Coatings

Prepared via Plasma Spray Process, *Appl. Surf. Sci.*, 2019, **478**, p 478–486.

15. M. Löbel, T. Lindner, S. Clauß, R. Pippig, D. Dietrich, and T. Lampke, Microstructure and Wear Behavior of the High-Velocity-Oxygen-Fuel Sprayed and Spark Plasma Sintered High-Entropy Alloy AlCrFeCoNi, *Adv. Eng. Mater.*, 2021, **23**(4), p 2001253.

16. A. Meghwal, A. Anupam, V. Luzin, C. Schulz, C. Hall, B.S. Murty, R.S. Kottada, C.C. Berndt, and A.S.M. Ang, Multiscale Mechanical Performance and Corrosion Behaviour of Plasma Sprayed AlCoCrFeNi High-Entropy Alloy Coatings, *J. Alloys Compd.*, 2021, **854**, p 157140.

17. A.S.M. Ang, C.C. Berndt, M.L. Sesso, A. Anupam, P. S, R.S. Kottada, and B.S. Murty, Plasma-Sprayed High Entropy Alloys: Microstructure and Properties of AlCoCrFeNi and MnCoCrFeNi, *Metall. Mater. Trans. A Phys. Metall. Mater. Sci.*, 2015, **46**(2), p 791–800.

18. L. Chen, K. Bobzin, Z. Zhou, L. Zhao, M. Öte, T. Königstein, Z. Tan, and D. He, Wear Behavior of HVOF-Sprayed Al0.6TiCrFeCoNi High Entropy Alloy Coatings at Different Temperatures, *Surf. Coatings Technol.*, 2019, **358**, p 215–222.

19. A. Meghwal, A. Anupam, B.S. Murty, C.C. Berndt, R.S. Kottada, and A.S.M. Ang, Thermal Spray High-Entropy Alloy Coatings: A Review, *J. Therm. Spray Technol.*, 2020, **29**(5), p 857–893.

20. B. Ganesh Reddy Majji, H. Vasudev, and A. Bansal, A Review on the Oxidation and Wear Behavior of the Thermally Sprayed High-Entropy Alloys, *Mater. Today Proc.*, 2021, **50**, p 1447–1451.

21. A. Sharma, High Entropy Alloy Coatings and Technology, *Coatings*, 2021, **11**(4), p 372.

22. B. Jin, N. Zhang, H. Yu, D. Hao, and Y. Ma, AlxCoCrFeNiSi High Entropy Alloy Coatings with High Microhardness and Improved Wear Resistance, *Surf. Coatings Technol.*, 2020, **402**, p 126328.

23. W.B. Liao, Z.X. Wu, W. Lu, M. He, T. Wang, Z. Guo, and J. Huang, Microstructures and Mechanical Properties of CoCrFeNiMn High-Entropy Alloy Coatings by Detonation Spraying, *Intermetallics*, 2021, **132**, p 107138.

24. Y. Xu, W. Li, L. Qu, X. Yang, B. Song, R. Lupoi, and S. Yin, Solid-State Cold Spraying of FeCoCrNiMn High-Entropy Alloy: An Insight into Microstructure Evolution and Oxidation Behavior at 700-900 °C, *J. Mater. Sci. Technol.*, 2021, **68**, p 172–183.

25. Y. Zhang, Y.J. Zhou, J.P. Lin, G.L. Chen, and P.K. Liaw, Solid-Solution Phase Formation Rules for Multi-Component Alloys, *Adv. Eng. Mater.*, 2008, **10**(6), p 534–538.

26. S. Guo, C. Ng, J. Lu, and C.T. Liu, Effect of Valence Electron Concentration on Stability of Fcc or Bcc Phase in High Entropy Alloys, *J. Appl. Phys.*, 2011, **109**(10), p 103505.

27. Y. Zhang, X. Chen, S. Jayalakshmi, R.A. Singh, V.B. Deev, and E.S. Prusov, Factors Determining Solid Solution Phase Formation and Stability in CoCrFeNiX0.4 (X=Al, Nb, Ta) High Entropy Alloys Fabricated by Powder Plasma Arc Additive Manufacturing, *J. Alloys Compd.*, 2021, **857**, p 157625.

28. M.G. Poletti, G. Fiore, B.A. Szost, and L. Battezzati, Search for High Entropy Alloys in the X-NbTaTiZr Systems (X = Al, Cr, V, Sn), *J. Alloys Compd.*, 2015, **620**, p 283–288.

29. U. Mizutani, Hume-Rothery Rules for Structurally Complex Alloy Phases, *MRS Bull.*, 2012, **37**(2), p 169–169.

30. J.B. Mann, T.L. Meek, and L.C. Allen, Configuration Energies of the Main Group Elements, *J. Am. Chem. Soc.*, 2000, **122**(12), p 2780–2783.

31. M.C. Gao, P.K. Liaw, J.W. Yeh, and Y. Zhang, "High-Entropy Alloys: Fundamentals and Applications," *High-Entropy Alloys: Fundamentals and Applications*, Springer International Publishing, 2016.

32. R. Feng, P.K. Liaw, M.C. Gao, and M. Widom, First-Principles Prediction of High-Entropy-Alloy Stability, *npj Comput. Mater.*, 2017, **3**(1).

33. S. Gorsse and F. Tancret, Current and Emerging Practices of CALPHAD toward the Development of High Entropy Alloys and Complex Concentrated Alloys, *J. Mater. Res.*, 2018, **33**(19), p 2899–2923.

34. C. Wen, Y. Zhang, C. Wang, D. Xue, Y. Bai, S. Antonov, L. Dai, T. Lookman, and Y. Su, Machine Learning Assisted Design of High Entropy Alloys with Desired Property, *Acta Mater.*, 2019, **170**, p 109–117.

35. Z. Zhou, Y. Zhou, Q. He, Z. Ding, F. Li, and Y. Yang, Machine Learning Guided Appraisal and Exploration of Phase Design for High Entropy Alloys, *npj Comput. Mater.*, 2019, **5**(1).

36. S.Y. Lee, S. Byeon, H.S. Kim, H. Jin, and S. Lee, Deep Learning-Based Phase Prediction of High-Entropy Alloys: Optimization, Generation, and Explanation, *Mater. Des.*, 2021, **197**, p 109260.

37. K. Kaufmann and K.S. Vecchio, Searching for High Entropy Alloys: A Machine Learning Approach, *Acta Mater.*, 2020, **198**, p 178–222.

38. J. Li, B. Xie, Q. Fang, B. Liu, Y. Liu, and P.K. Liaw, High-Throughput Simulation Combined Machine Learning Search for Optimum Elemental Composition in Medium Entropy Alloy, *J. Mater. Sci. Technol.*, 2021, **68**, p 70–75.

39. C. Chattopadhyay, A. Prasad, and B.S. Murty, Phase Prediction in High Entropy Alloys – A Kinetic Approach, *Acta Mater.*, 2018, **153**, p 214–225.

40. L. Breiman, Random Forests, *Mach. Learn.*, 2001, **45**, p 5–32.

41. F. Pedregosa, V. Michel, O. Grisel, M. Blondel, P. Prettenhofer, R. Weiss, J. Vanderplas, D. Cournapeau, F. Pedregosa, G. Varoquaux, A. Gramfort, B. Thirion, O. Grisel, V. Dubourg, A. Passos, M. Brucher, M. Perrot, and É. Duchesnay, Scikit-Learn: Machine Learning in Python, *J. Mach. Learn. Res.*, 2011, **12**, p 2825–2830.

42. A.O. Oliynyk, E. Antono, T.D. Sparks, L. Ghadbeigi, M.W. Gaultois, B. Meredig, and A. Mar, High-Throughput Machine-Learning-Driven Synthesis of Full-Heusler Compounds, *Chem. Mater.*, 2016, **28**(20), p 7324–7331.

43. W. Huang, P. Martin, and H.L. Zhuang, Machine-Learning Phase Prediction of High-Entropy Alloys, *Acta Mater.*, 2019, **169**, p 225–236.

44. J.R. Davis, "Handbook of Thermal Spray Technology," *Technology*, ASM International, 2004.

45. L. Bianchi, A.C. Leger, M. Vardelle, A. Vardelle, and P. Fauchais, Splat Formation and Cooling of Plasma-Sprayed Zirconia, *Thin Solid Films*, 1997, **305**(1–2), p 35–47.

46. L. van der Maaten and G. Hinton, Visualizing Data Using T-SNE Laurens, *J. Mach. Learn. Res.*, 2008, **9**, p 2579–2605.

47. S. Singh, N. Wanderka, K. Kiefer, K. Siemensmeyer, and J. Banhart, Effect of Decomposition of the Cr-Fe-Co Rich Phase of AlCoCrCuFeNi High Entropy Alloy on Magnetic Properties, *Ultramicroscopy*, 2011, **111**(6), p 619–622.

48. K.G. Pradeep, N. Wanderka, P. Choi, J. Banhart, B.S. Murty, and D. Raabe, Atomic-Scale Compositional Characterization of a Nanocrystalline AlCrCuFeNiZn High-Entropy Alloy Using Atom Probe Tomography, *Acta Mater.*, 2013, **61**(12), p 4696–4706.

49. A. Manzoni, H. Daoud, R. Völkl, U. Glatzel, and N. Wanderka, Phase Separation in Equiatomic AlCoCrFeNi High-Entropy Alloy, *Ultramicroscopy*, 2013, **132**, p 212–215.

50. X.D. Xu, P. Liu, S. Guo, A. Hirata, T. Fujita, T.G. Nieh, C.T. Liu, and M.W. Chen, Nanoscale Phase Separation in a Fcc-Based CoCrCuFeNiAl0.5 High-Entropy Alloy, *Acta Mater.*, 2015, **84**, p 145–152.

51. Y. Yue, R. Von der Ohe, and S.L. Jensen, Fictive Temperature, Cooling Rate, and Viscosity of Glasses, *J. Chem. Phys.*, 2004, **120**(17), p 8053–8059.

52. L. Grunberg and A.H. Nissan, Mixture Law for Viscosity, *Nature*, 1949, **164**(4175), p 799–800.

53. I. Budai, M.Z. Benkő, and G. Kaptay, Comparison of Different Theoretical Models to Experimental Data on Viscosity of Binary Liquid Alloys, *Mater. Sci. Forum*, 2007, **537**–**538**, p 489–496.

54. A.R. Miedema, R. Boom, and F.R. De Boer, On the Heat of Formation of Solid Alloys, *J. Less-Common Met.*, 1975, **41**(2), p 283–298.

55. E.A. Brandes and G.B. Brook, "Smithells Metals Reference Book: Seventh Edition," *Smithells Metals Reference Book: Seventh Edition*, Elsevier, 2013.

56. T. Ishikawa, P.F. Paradis, J.T. Okada, M.V. Kumar, and Y. Watanabe, Viscosity of Molten Mo, Ta, Os, Re, and W Measured by Electrostatic Levitation, *J. Chem. Thermodyn.*, 2013, **65**, p 1–6.

57. L. Battezzati and A.L. Greer, The Viscosity of Liquid Metals and Alloys, *Acta Metall.*, 1989, **37**(7), p 1791–1802.

58. M. Löbel, T. Lindner, R. Pippig, and T. Lampke, High-Temperature Wear Behaviour of Spark Plasma Sintered AlCoCrFeNiTi0.5 High-Entropy Alloy, *Entropy*, 2019, **21**(6), p 582.

59. C. Chen, Y. Fan, W. Wang, H. Zhang, J. Hou, R. Wei, T. Zhang, T. Wang, M. Li, S. Guan, and F. Li, Synthesis of Ultrafine Dual-Phase Structure in CrFeCoNiAl0.6 High Entropy Alloy via Solid-State Phase Transformation during Sub-Rapid Solidification,

J. Mater. Sci. Technol., 2022, **113**, p 253–260.

60. F. He, Z. Wang, Y. Li, Q. Wu, J. Li, J. Wang, and C.T. Liu, Kinetic Ways of Tailoring Phases in High Entropy Alloys, *Sci. Rep.*, 2016, **6**(1).

61. N. Zeoli, H. Tabbara, and S. Gu, Three-Dimensional Simulation of Primary Break-up in a Close-Coupled Atomizer, *Appl. Phys. A Mater. Sci. Process.*, 2012, **108**(4), p 783–792.

62. N. Zeoli and S. Gu, Computational Simulation of Metal Droplet Break-up, Cooling and Solidification during Gas Atomisation, *Comput. Mater. Sci.*, 2008, **43**(2), p 268–278.

Figure Captions

Figure 1. a) t-SNE projection of cooling dataset without new feature construction, b) Original dataset without cooling rate entries.

Figure 2. Pair-plot of two model features, the Ionisation Energy and the Latent Heat. The population is a univariate distribution plot drawn to show the marginal distribution of the data.

Figure 3. ROC Curve of the model including the new Sk feature.

Figure 4. Random Forest model decision plot showing the Sk and VEC pair rules for phase formation under different cooling rates expressed through the new Sk feature.

Figure 5. Confusion matrix of the Random Forest multiple phase formation classification

Figure 6. As Cast High Entropy alloys (a) XRDs of the Cantor Alloy showing single phase FCC structure and modified Cantor with the addition of Vanadium showing FCC plus secondary phases, (b) EDS showing uniform distribution of elements in the Vanadium containing alloy, (c) EDS showing the distribution of elements in the original Cantor Alloy.

Figure 7. Atomised CoCrFeMnNi0.8V alloy powder. (a) XRDs showing a single BCC phase as opposed to FCC+Sec in the as cast material. (b) Powder morphology, (c) EDS.

Figure 8. Thermal Spray via Atmospheric Plasma Spray (APS). (a) XRDs showing FCC and BCC for the APS sprayed CantorV (CoCrFeMnNi0.8V) alloy and lamella coating microstructure with oxide formation, (b) XRDs showing primary FCC formation with oxides for the APS sprayed original Cantor alloy (CoCrFeMnNi) and lamella coating microstructure with oxide formation.

Figure 9. Thermal Spray via High Velocity Oxy-Fuel (HVOF). (a) XRDs showing single BCC phase for the HVOF sprayed CantorV and coating microstructure. (b) XRDs showing single FCC phase for the HVOF sprayed original Cantor Alloy and coating microstructure.

1
2
3
4
5
6
7
8
9
10
11
12
13
14
15
16
17
18
19
20
21
22
23
24
25
26
27
28
29
30
31
32
33
34
35
36
37
38
39
40
41
42
43
44
45
46
47
48
49
50
51
52
53
54
55
56
57
58
59
60

Table 1. A list of first ten features used to train the model ranked by importance scores. Importance scores are representative of a given feature's contribution to the model's performance.

Feature Importance	
S_k (New Feature from this work)	9%
Mean of Number of d valence electrons for formula (Citrination Generated)	4%
Mean of Conduction ionization energy for formula (Citrination Generated)	4%
Mean of Radius of d orbitals for formula (Citrination Generated)	4%
Mean of Elemental work function for formula (Citrination Generated)	3%
Mean of Elemental atomic volume for formula (Citrination Generated)	3%
Mean of Packing density for formula (Citrination Generated)	3%
Mean of Total number of unfilled valence electrons for formula (Citrination Generated)	3%
Mean of Elemental density for formula (Citrination Generated)	2%
Mean of Valence electron density for formula (Citrination Generated)	2%

Table 2. Model Accuracy (81%) for the binary FCC/BCC phase classification for a given HEA composition under different cooling rates.

	Precision	Recall	F1-Score
Accuracy	-	-	0.81
Macro Avg.	0.84	0.84	0.81
Weighted Avg.	0.87	0.81	0.81

Table 3. Phase formation model predictions during gas atomization and coating deposition and comparisons with experimental findings.

Oxide formation is excluded from Model Predictions, Arc-Melting Cooling Rate = 100-1000K/s, APS Deposition Re-Solidifcaiton Cooling Rate Up to 10^8 K/s, Atromisation Cooling Rate Up to 10^7 K/s						
Material	Predicted as Cast	Exp. Feedstock	Predicted Feedstock	Predicted Coating Phases	Exp. Coating Phases	Ref.
AlSiTiCrFeCoNiMo0.5	BCC+Sec (Arc-Melting)	BCC+FCC (Arc-Melting+Ball Milling)	BCC+Sec (Arc-Melting)	BCC (APS)	BCC (APS)	[58]
AlSiTiCrFeNiMo0.5	BCC+Sec (Arc-Melting)	BCC+FCC (Arc-Melting+Ball Milling)	BBC (Arc-Melting)	BCC (APS)	BCC (APS)	[58]
AlSiTi0.2Cr1.5Fe0.2Co0.6Ni	BCC+Sec (Arc-Melting)	BCC+Sec (Arc-Melting+Ball Milling)	BCC+Sec (Arc-Melting)	BCC+B2 (APS)	BCC+Sec (APS)	[59]
CoCrFeMnNi	FCC (Arc-Melting)	FCC (Atomisation)	FCC (Atomisation)	FCC (APS)	FCC (APS)	This work
CoCrFeMnNi	FCC (Arc-Melting)	FCC+minorBCC (Mechanical Alloying)	FCC (Arc-Melting)	FCC (APS)	FCC(APS)	[17]
AlTiCrFeCoNi	BCC (Arc-Melting)	BCC (Mechanical Alloying)	BCC (Arc-Melting)	BCC (APS)	BCC+minor FCC (APS)	[60]
AlTiCrFeCoNi	BCC (Arc-Melting)	BCC (Atomisation)	BCC (Atomisation)	BCC (APS)	BCC+BCC (APS)	[61]
CrFeCoNiMo0.2	FCC (Arc-Melting)	FCC (Atomisation)	FCC (Atomisation)	FCC (APS)	FCC (APS)	[62]
AlSiTi0.2Cr1.5Fe0.2Co0.6Ni	BCC (Arc-Melting)	BCC+FCC (Atomisation)	BCC (Atomisation)	BCC+B2 (APS)	BCC+FCC+Other	[63]
AlSiCr1.3Fe0.2Co0.6Ni	BCC+B2 (Arc-Melting)	BCC+FCC (Atomisation)	BCC (Atomisation)	BCC (APS)	BCC+FCC+Other	[63]
AlCrFeCoNi	BCC+B2 (Arc-Melting)	BCC+B2 (Atomisation)	BCC+B2 (Atomisation)	BCC+B2 (APS)	BCC+B2+FCC	[14]
CoCrFeMnNi0.8V	FCC+Sec (Arc-Melting)	BCC (Atomisation)	BCC (Atomisation)	FCC+BCC (APS), BCC (HVOF)	FCC+BCC (APS), BCC (HVOF)	This work

Table 4. The chemical composition and phase formation of the bulk as-cast, powder and coating materials.

Sample	Co at%	Cr at%	Fe at%	Mn at%	Ni at%	V at%	Structure
Cantor Nominal	20	20	20	20	20	0	-
As-Cast Cantor Measured	21.4 ± 1.2	17.2 ± 0.6	20.4 ± 1.1	20.6 ± 0.7	20.4 ±1.2	0	FCC
CantorV Nominal	17.2	17.2	17.2	17.2	13.8	17.2	-
As-Cast CantorV Measured	16.6 ± 0.8	19.1 ± 3.5	18.2 ± 1.8	15.7 ± 1.3	17.4 ± 2.1	13.1 ± 1.2	FCC+σ
Powder Cantor Measured	18.9 ± 0.7	21.3 ± 0.4	20 ± 0.4	21.9 ± 1.1	17.9 ± 0.5	0	FCC
Powder CantorV Measured	17.3 ± 0.4	18.1 ± 0.3	17.1 ± 0.1	17.9 ± 0.5	13.8 ± 0.2	15.9 ± 0.3	BCC
HVOF Coating Cantor Measured	20.9 ± 0.5	18.6 ± 0.6	20 ± 0.9	19.5 ± 0.8	21± 1.1	0	FCC
Plasma Coating Cantor Measured	20.2 ± 0.6	21.5 ± 0.5	21.8 ± 1.5	13.8 ± 0.7	20.8 ± 0.2	0	FCC
HVOF Coating CantorV Measured	17.4 ± 0.1	18.3 ± 0.2	17.1 ± 0.3	17.6 ± 0.1	13.8 ± 0.1	15.9 ± 0.3	BCC
Plasma Coating CantorV Measured	18.8 ± 1.1	19.5 ± 1.2	18.4 ± 0.1	10.9 ± 0.4	14.4 ± 0.3	18.1 ± 0.4	FCC+BCC
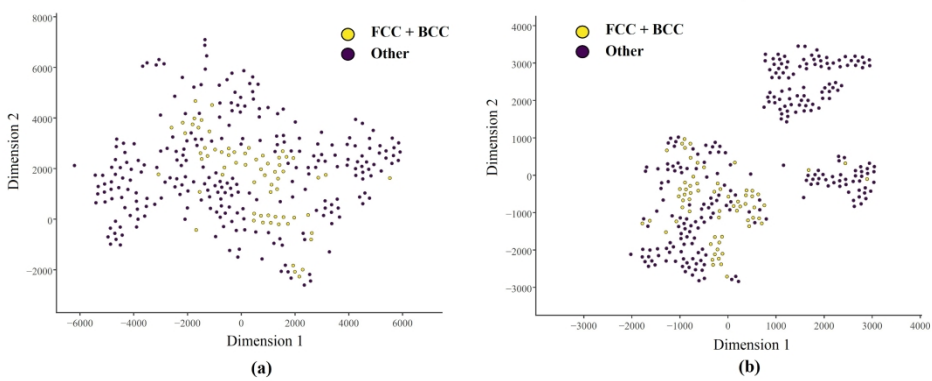
Figure 1. a) t-SNE projection of cooling dataset without new feature construction, b) Original dataset without cooling rate entries.
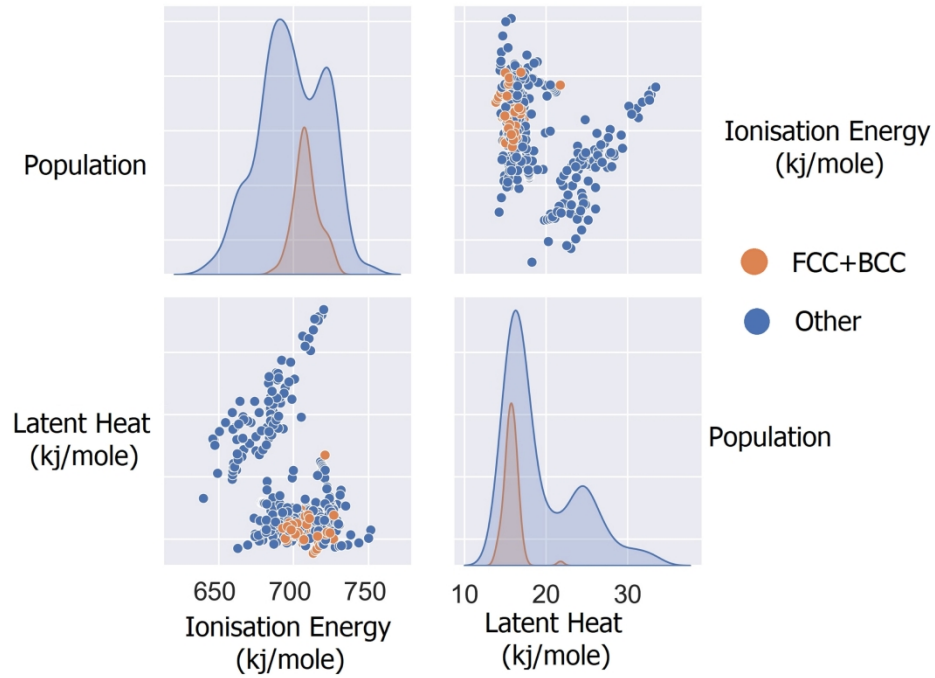
580x241mm (300 x 300 DPI)

1
2
3
4
5
6
7
8
9
10
11
12
13
14
15
16
17
18
19
20
21
22
23
24
25
26
27
28
29
30
31
32
33
34
35
36
37
38
39
40
41
42
43
44
45
46
47
48
49
50
51
52
53
54
55
56
57
58
59
60

Figure 2. Pair-plot of two model features, the Ionisation Energy and the Latent Heat. The population is a univariate distribution plot drawn to show the marginal distribution of the data.

304x241mm (300 x 300 DPI)
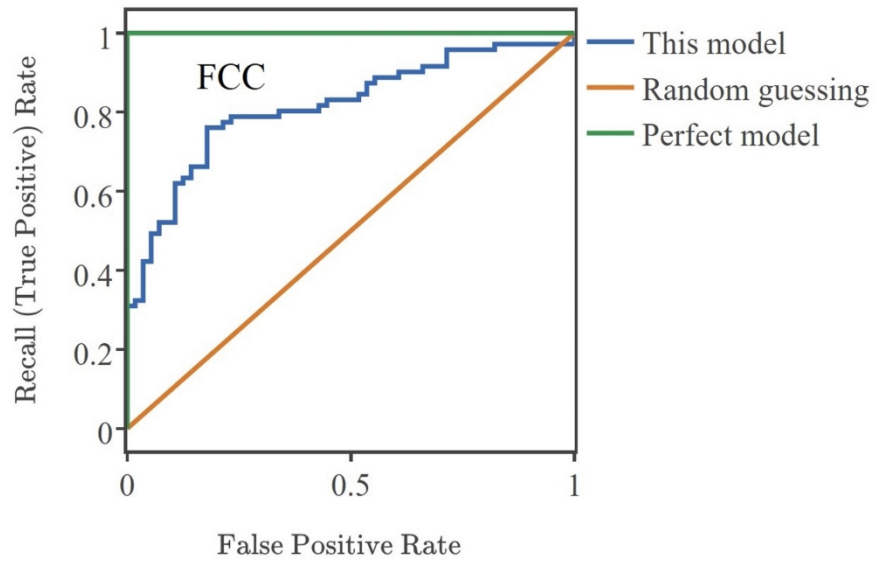
Figure 3. ROC Curve of the model including the new Sk feature.

304x220mm (300 x 300 DPI)
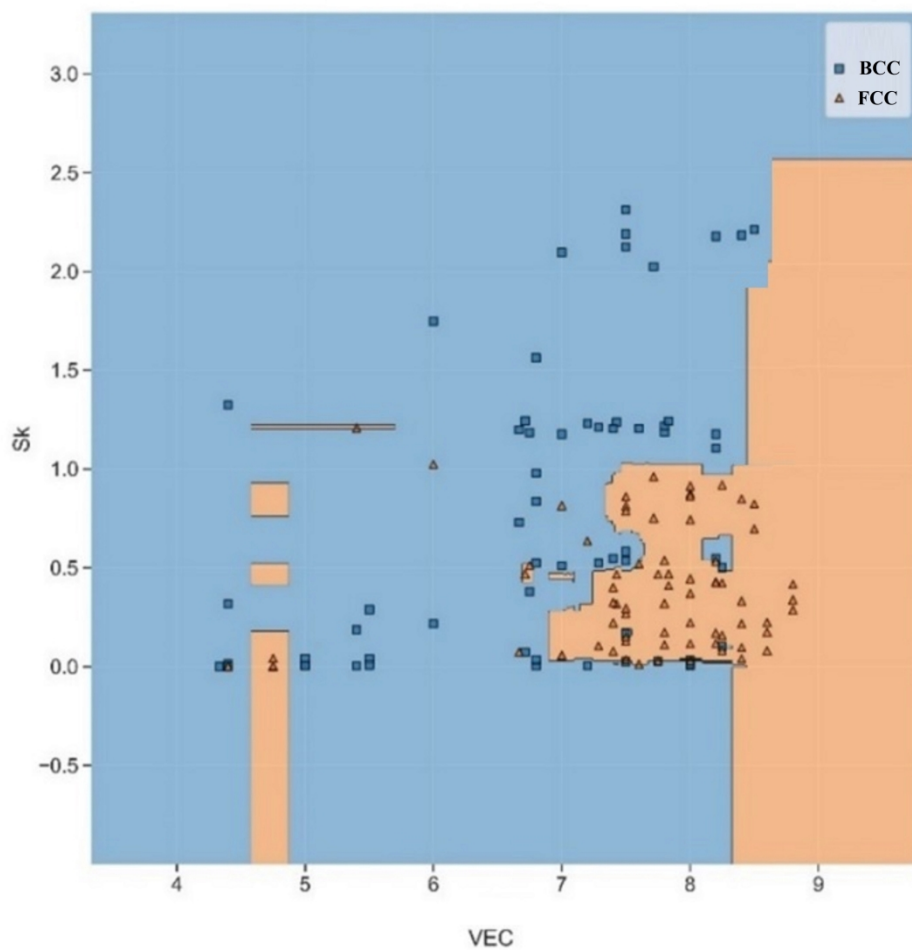
Figure 4. Random Forest model decision plot showing the Sk and VEC pair rules for phase formation under different cooling rates expressed through the new Sk feature.
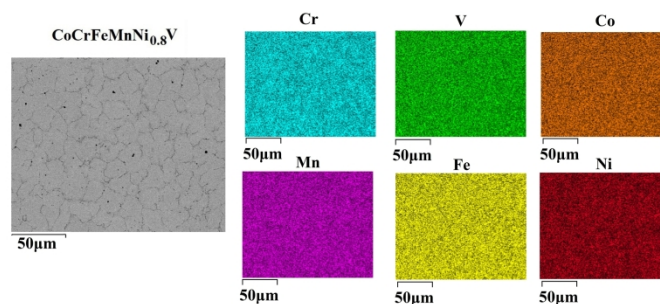
444x436mm (300 x 300 DPI)
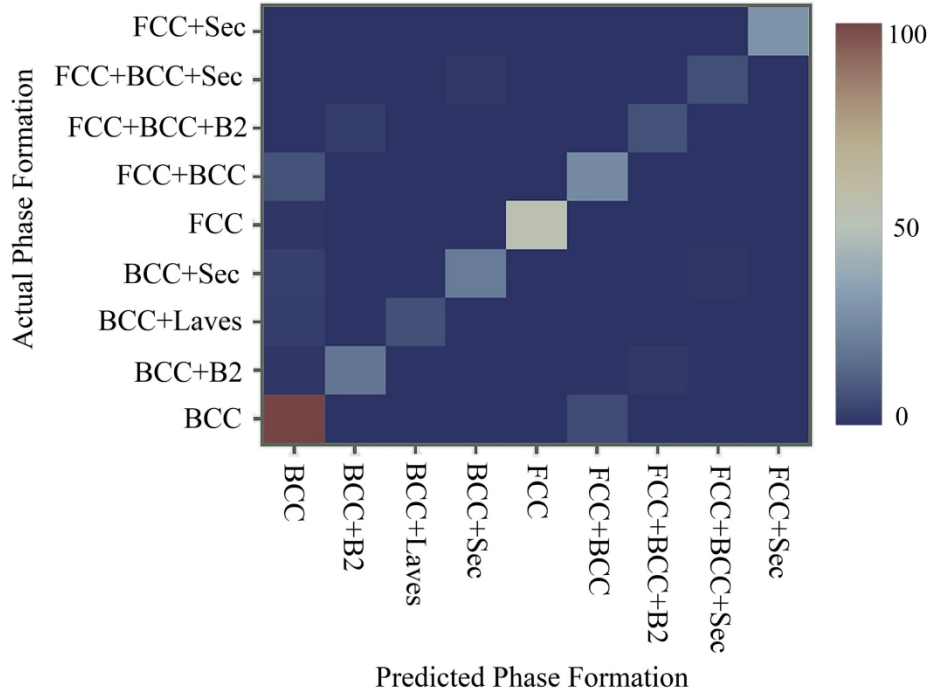
Figure 5. Confusion matrix of the Random Forest multiple phase formation classification

152x124mm (600 x 600 DPI)
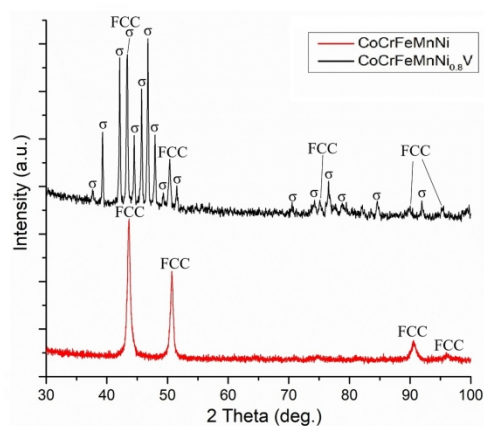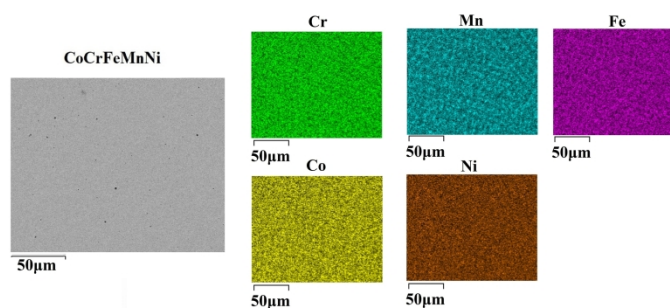
Figure 6. As Cast High Entropy alloys (a) XRDs of the Cantor Alloy showing single phase FCC structure and modified Cantor with the addition of Vanadium showing FCC plus secondary phases, (b) EDS showing uniform distribution of elements in the Vanadium containing alloy, (c) EDS showing the distribution of elements in the original Cantor Alloy.

239x355mm (300 x 300 DPI)

1
2
3
4
5
6
7
8
9
10
11
12
13
14
15
16
17
18
19
20
21
22
23
24
25
26
27
28
29
30
31
32
33
34
35
36
37
38
39
40
41
42
43
44
45
46
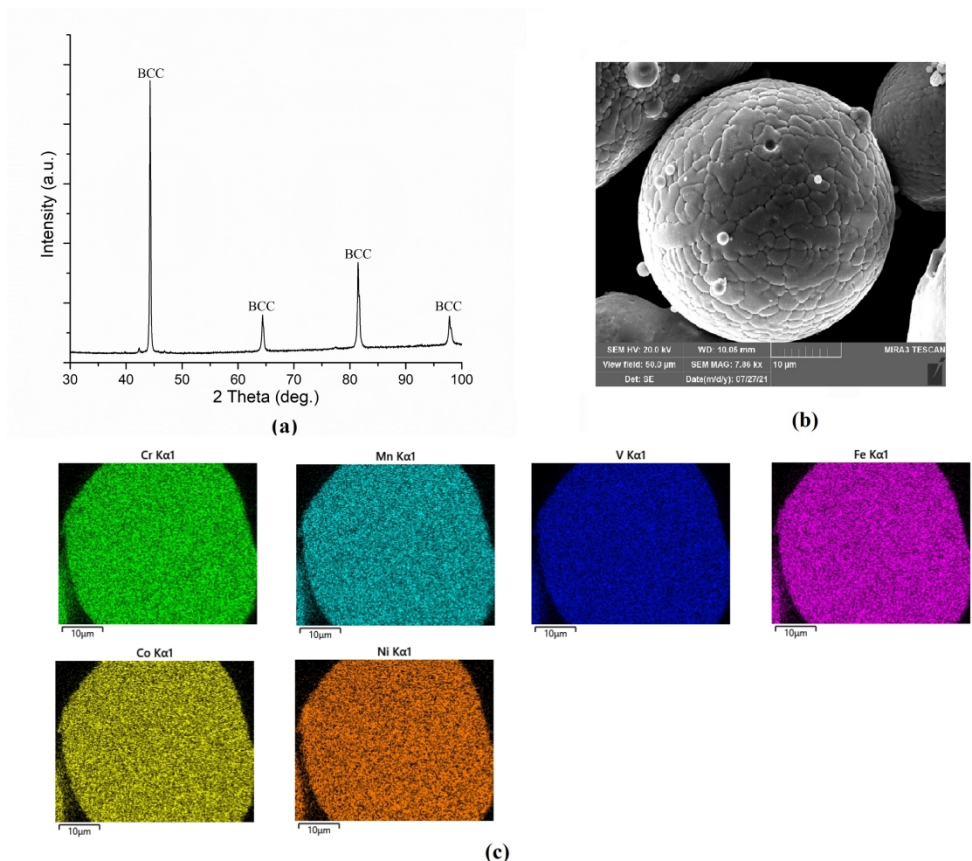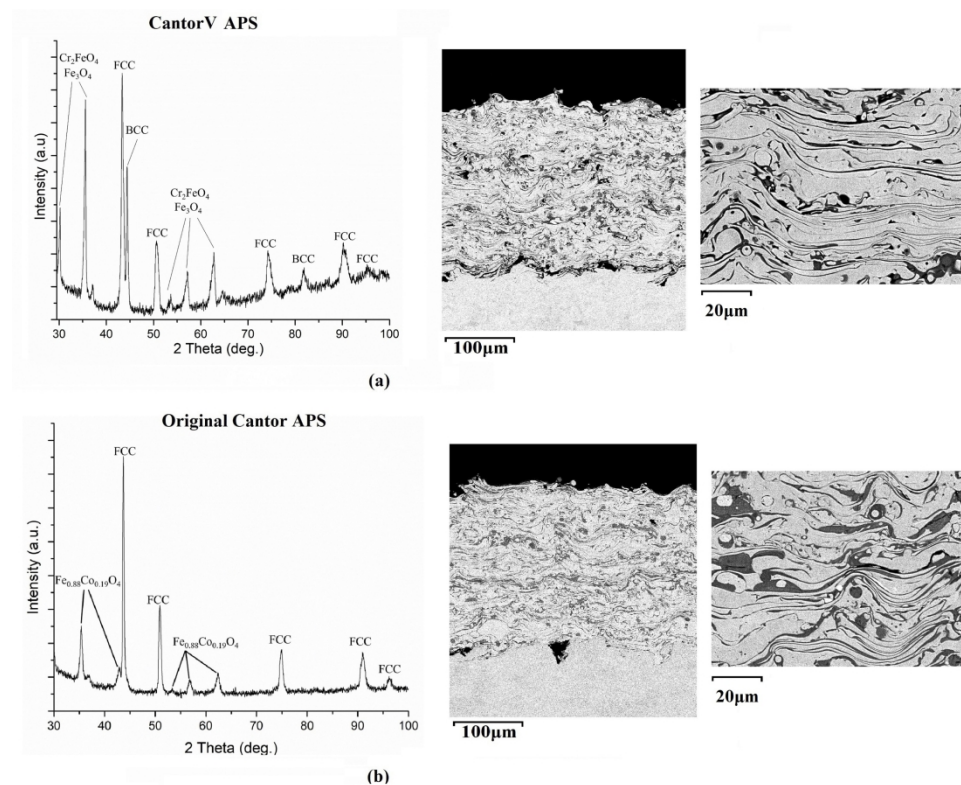47
48
49
50
51
52
53
54
55
56
57
58
59
60

Figure 7. Atomised CoCrFeMnNi0.8V alloy powder. (a) XRDs showing a single BCC phase as opposed to FCC+Sec in the as cast material. (b) Powder morphology, (c) EDS.

327x286mm (300 x 300 DPI)

Figure 8. Thermal Spray via Atmospheric Plasma Spray (APS). (a) XRDs showing FCC and BCC for the APS sprayed CantorV (CoCrFeMnNi0.8V) alloy and lamella coating microstructure with oxide formation, (b) XRDs showing primary FCC formation with oxides for the APS sprayed original Cantor alloy (CoCrFeMnNi) and lamella coating microstructure with oxide formation.
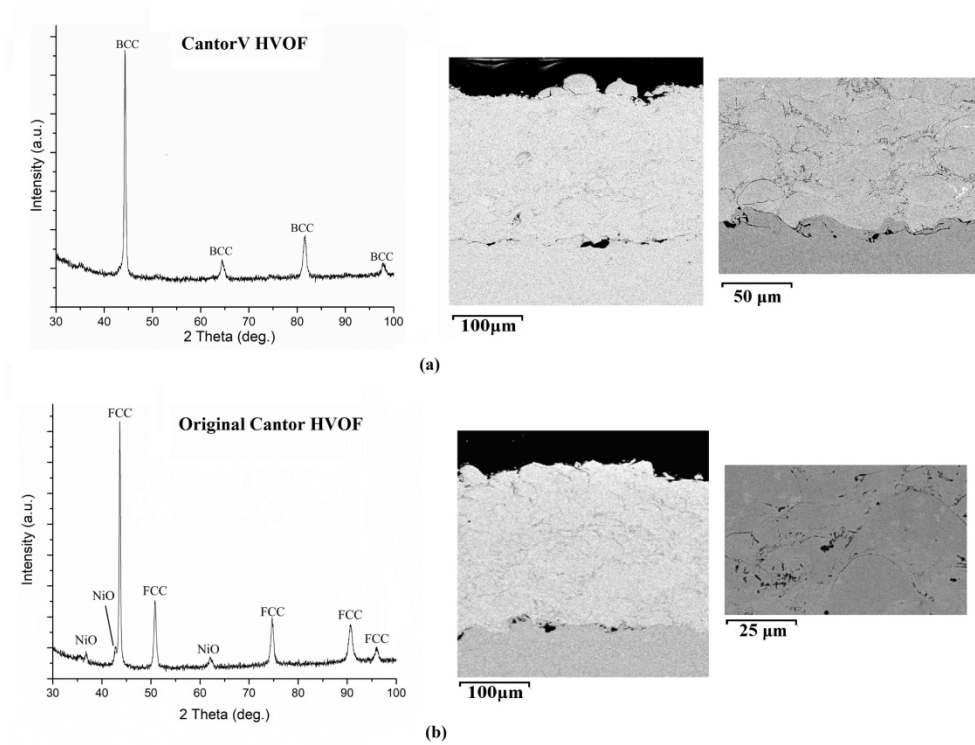
146x119mm (600 x 600 DPI)

Figure 9. Thermal Spray via High Velocity Oxy-Fuel (HVOF). (a) XRDs showing single BCC phase for the HVOF sprayed CantorV and coating microstructure. (b) XRDs showing single FCC phase for the HVOF sprayed original Cantor Alloy and coating microstructure.

143x109mm (600 x 600 DPI)